

Probing the dynamical state, baryon content, and multiphase nature of galaxy clusters with bright background QSOs

Chong Ge^{1,2,3,4}, Q. Daniel Wang^{5*}, Joseph N. Burchett⁵, Todd M. Tripp⁵, Ming Sun⁴, Zhiyuan Li^{3,6,7}, Qiusheng Gu^{3,6,7} and Li Ji^{1,2}

¹*Purple Mountain Observatory, Chinese Academy of Sciences, Nanjing 210008, China*

²*Key Laboratory of Dark Matter and Space Astronomy, PMO, CAS, Nanjing 210008, China*

³*Key Laboratory of Modern Astronomy and Astrophysics (Nanjing University), Ministry of Education, Nanjing 210093, China*

⁴*Department of Physics and Astronomy, University of Alabama in Huntsville, Huntsville, AL 35899, USA*

⁵*Department of Astronomy, University of Massachusetts, Amherst, MA 01003, USA*

⁶*School of Astronomy and Space Science, Nanjing University, Nanjing 210093, China*

⁷*Collaborative Innovation Center of Modern Astronomy and Space Exploration, Nanjing 210093, China*

Accepted. Received; in original form

ABSTRACT

We have initiated a programme to study the physical/dynamical state of gas in galaxy clusters and the impact of the cluster environment on gaseous halos of individual galaxies using X-ray imaging and UV absorption line spectroscopy of background QSOs. Here we report results from the analysis *Chandra* and *XMM-Newton* archival data of five galaxy clusters with such QSOs, one of which has an archival UV spectrum. We characterize the gravitational masses and dynamical states, as well as the hot intracluster medium (ICM) properties of these clusters. Most clusters are dynamically disturbed clusters based on the X-ray morphology parameters, the X-ray temperature profiles, the large offset between X-ray peak and brightest cluster galaxy (BCG). The baryon contents in the hot ICM and stars of these clusters within r_{500} are lower than the values expected from the gravitational masses, according to the standard cosmology. We also estimate column densities of the hot ICM along the sightlines toward the background QSOs as well as place upper limits on the warm-hot phase for the one sightline with existing UV observations. These column densities, compared with those of the warm and warm-hot ICM to be measured with UV absorption line spectroscopy, will enable us to probe the relationship among various gaseous phases and their connection to the heating/cooling and dynamical processes of the clusters. Furthermore, our analysis of the archival QSO spectrum probing one cluster underscores the need for high quality, targeted UV observations to robustly constrain the 10^{5-6} K gas phase.

Key words: galaxies: clusters: general –galaxies: clusters: intracluster medium– X-rays: galaxies: clusters–quasars: absorption lines.

1 INTRODUCTION

Diffuse X-ray emission is routinely observed from the hot intracluster medium (ICM) of galaxy clusters. This emission arises chiefly in their inner regions ($r \lesssim r_{500}$, within which the mean mass density is 500 times the critical density of the Universe). Recently, however, diffuse X-ray emission has also been observed from outer regions of rich clusters as well (e.g., Bonamente et al. 2012; Eckert et al. 2012; Walker et al. 2013; Wang & Walker 2014). These observations indicate that the ICM is inhomogeneous, especially in outer regions, as predicted by theoretical models or simulations

of structure formation (e.g., Roncarelli et al. 2006; Molnar et al. 2009), which show a complicated shock heating/cooling history in the outer ICM regions (out to a few r_{200} , where the strong external shock of the accretion flow is located, e.g., Molnar et al. 2009) and an enhanced presence of the multiphase warm-hot plasma may be expected (e.g., Pfrommer et al. 2008). In addition, the cluster environment could strongly affect the circumgalactic medium (CGM) of individual galaxies via processes such as ram-pressure stripping and pressure compression (e.g. Lu & Wang 2011; Emerick et al. 2015; Roediger et al. 2015). However, the effectiveness of such stripping remains greatly uncertain, especially in outer regions of clusters, as demonstrated in recent simulations, where the existence of a complex pattern of flows, turbulence, and a continuous fueling

* E-mail: wqd@astro.umass.edu

of the CGM from the ICM is considered (e.g., [Quilis et al. 2017](#)). New observational constraints are needed to make progress in our understanding of these phenomena and physical processes, which are important not only for determining the properties of the ICM and the effects on galaxy evolution, but also for properly using clusters as cosmology probes (e.g., via the Sunyaev-Zel'dovich effect).

We have been conducting a multi-wavelength study of how the properties of the ICM and CGM may be affected by the richness and dynamical state of galaxy clusters (e.g., [Wang & Walker 2014](#); [Ge et al. 2016](#); [Burchett et al. 2018](#)). We use 1) X-ray observations to characterize the morphological and thermal properties of the hot ICM, 2) far-UV absorption-line spectroscopy to constrain the column densities, metal abundances, and kinematics of warm and warm-hot gas, and 3) optical spectroscopy of galaxies to determine their associations with individual absorbers and X-ray-emitting substructures.

Our initial studies were focused on a few optically selected clusters, as reported in [Wang & Walker \(2014\)](#), [Ge et al. \(2016\)](#), and [Burchett et al. \(2018\)](#). These studies are based on archival *Chandra* data as well as new *XMM-Newton* and *Hubble Space Telescope (HST)/Cosmic Origins Spectrograph (COS)* observations. [Wang & Walker \(2014\)](#) show how the density and temperature radial profiles (hence the hot gas properties of individual clusters along the QSO sightline) can be estimated even when the X-ray emission from the projected clusters is present. Based on *XMM-Newton* observations, [Ge et al. \(2016\)](#) find that each of the two optically-selected clusters actually consists of distinct merging subcluster pairs at similar redshifts. These subclusters themselves typically show substantial substructures, including strongly distorted radio lobes, as well as large position offsets between the diffuse X-ray centroids and the brightest galaxies. Thus these clusters are dynamically young systems. Comparing the hot gas and stellar masses of each cluster with the expected cosmological baryonic mass fraction indicates a significant deficit, which could be filled by other gas components ([Ge et al. 2016](#)).

[Burchett et al. \(2018\)](#) present the *HST/COS* study of these clusters. They detect broad Ly α absorption (BLA) features associated with one cluster. However, rather than tracing material contained within the ICM, these features are consistent with metal-poor material in-falling from the intergalactic medium (IGM). Another QSO sightline probes the interface region of a dynamically young system of merging subclusters and shows a quite narrow $b \sim 16 \text{ km s}^{-1}$ H I profile at the cluster system's redshift, which may represent a dense, cool ($T \sim 10^4 \text{ K}$) cloudlet induced in the wake of the cluster merger shock. Interestingly, no OVI is detected to sensitive limits [$N(\text{OVI}) \lesssim 10^{13.7} \text{ cm}^{-2}$]. While these results are intriguing, it is still difficult to make any firm conclusions regarding the multi-phase ICM properties of galaxy clusters in general, let alone their baryon contents. The sample of seven clusters (including the newly discovered merging subclusters) that we have studied in these works is still too limited to allow a meaningful statistical analysis. These clusters are dominated by highly disturbed ones or even ongoing mergers. It is highly desirable to expand this sample to include more clusters that are relatively isolated and relaxed and that, of course, have UV-bright background QSOs at various impact parameters so that we can assess how the multi-phase ICM properties may depend on the cluster dynamical state.

Here, we present a study of a sample of relatively isolated X-ray-selected clusters, which are paired with UV-bright background QSOs. This study focuses primarily on the analysis of archival *Chandra* and *XMM-Newton* data, representing a step to enable a statistically meaningful investigation of the multiphase ICM and

Table 1. *Chandra* and *XMM-Newton* observations

Name	Obs-ID	Exp (ks)	Clean Exp (ks)
J0350	7227 (ACIS-I)	24.7	18.6
A655	15159 (ACIS-I)	8.0	7.2
A959	0406630201 (EPIC)	25.6/23.8/23.8 ^a	3.3/7.9/8.1
A1084	0201901501 (EPIC)	25.2/29.2/29.2	17.4/23.9/24.1
A2813	0042340201 (EPIC)	10.0/14.4/14.4	5.7/10.7/10.7

^aEPIC exposures of the pn/MOS1/MOS2 cameras.

CGM in and around clusters of galaxies. One of the clusters' background QSOs has been observed with *HST/COS*, and we analyze this spectrum to constrain the baryon contribution of warm-hot 10^{5-6} K gas to the cluster's baryon budget and demonstrate the need for targeted, high quality observations to address this scientific goal. The rest of the present paper is organized as follows: In Section 2 we describe the sample selection and our data reduction procedures; Section 3 presents the results based on the X-ray observations; Section 4 discusses the dynamical state and baryon content of clusters. Section 5 summarizes our results. We use the standard cold dark matter cosmology with $H_0 = 70 \text{ km s}^{-1} \text{ Mpc}^{-1}$, $\Omega_m = 0.3$, and $\Omega_\Lambda = 0.7$.

2 SAMPLE SELECTION AND X-RAY DATA ANALYSIS

2.1 Sample selection

We find our sample pairs for the present study from cross-correlating FUV-bright QSOs with a meta-catalog of X-ray-detected galaxy clusters ([Piffaretti et al. 2011](#)). We select clusters with $0.1 \leq z_c \leq 0.4$ and $kT \geq 2 \text{ keV}$, paired with UV-bright background QSOs of $m_{FUV} < 18.3$ and projected within $1.5 \times r_{200}$. In this redshift range, the warm and warm-hot ICM can be effectively observed with the COS to detect absorption lines of the O VI doublet, H I Ly α and Ly β , and a number of other ions. These lines uniquely constrain the thermal, kinematic, and chemical properties of cooler ICM/CGM gases at various cluster impact parameters. This redshift range is also ideal for weak lensing mapping of the gravitational mass distribution, Sunyaev-Zel'dovich effect measurements, multi-object galaxy spectroscopy, and X-ray imaging/spectroscopy of the hot ICM across the entire clusters. Here we focus on five galaxy clusters for which good-quality archival *Chandra* and *XMM-Newton* observations are available (Table 1). None of these clusters have been carefully analyzed in the literature, except for inclusions in some large surveys focused on scaling relations and cosmology (e.g., [Böhlinger et al. 2007](#); [Mahdavi et al. 2013](#); [Mantz et al. 2015](#)).

2.2 Chandra data

Two clusters were observed with the *Chandra/ACIS-I* (Table 1). We use *Chandra* Interactive Analysis of Observation (CIAO, version 4.7) and calibration database (CALDB, version 4.6.9) to reprocess the *Chandra* data, following a procedure similar to that detailed in [Wang & Walker \(2014\)](#). For each observation, we first reprocess a new level = 2 event file, using `chandra_repro` script with VFaint mode correction, and then clean time intervals strongly affected by flares, using the `deflare` script. Such intervals are defined to be first deviating more than 3σ and then a factor of ≥ 1.2 from the mean rate. The light curve is extracted from a bright

source-free region in the 2.3–7.3 keV band, which is most sensitive to flares due to both the spectral shapes of the flaring and the minimum quiescent instrument plus sky backgrounds (Hickox & Markevitch 2006). The exposure times of the clean data, as well as the original ones, are included in Table 1. We use `wavdetect` to detect discrete sources. The standard stowed background events are reprojected to match each of the two ACIS-I observations. The event rate of the background is rescaled to the count rate in the 9–12 keV band, where the *Chandra* effective area is negligible and the flux is dominated by the particle background.

We construct the count, stowed background, and effective exposure map in the 0.5–2.0 keV band, where the X-ray emission is dominated by the clusters. The background subtracted and exposure corrected intensity maps are then generated and smoothed with a $10''$ sigma Gaussian kernel using `aconvolve`.

The spectra are extracted with `specextract`. For the spectral fitting, we firstly subtract the instrumental background, and secondly subtract the sky background. The instrumental non-X-ray background spectra for the on-cluster spectra are estimated with the rescaled stowed data in the same detector regions. For the diffuse X-ray sky contribution, we use the HEASARC X-ray Background Tool to extract an off-cluster *ROSAT* all-sky survey (RASS) spectrum in an annulus (of inner and outer radii equal to 1–2 degree) around the cluster. We then jointly fit the non-X-ray background-subtracted on- and RASS off-cluster spectra. The off-cluster spectrum is fitted with a 3-component model consisting of an unabsorbed thermal model `apec` (for the Local Bubble contribution), an absorbed `apec` (the Galactic halo gas) and an absorbed `power-law` (the extragalactic background). In addition to this 3-component model, an additional absorbed `apec` (representing the cluster emission) is included to fit the on-cluster spectrum. Fig. A1 shows the relation between derived on-cluster soft sky flux and off-cluster RASS flux, they are correlated as expected (Sun et al. 2009).

2.3 XMM-Newton data

The *XMM-Newton* data used here are from the European Photon Imaging Camera (EPIC) consisting of two MOS and one pn CCD arrays. We process the data using the Extended Source Analysis Software (ESAS; Kuntz & Snowden 2008; Snowden et al. 2008), integrated into the *XMM-Newton* Science Analysis System (SAS, version 13.5.0.) with the associated Current Calibration Files (CCF), following the procedures detailed in Ge et al. (2016). Briefly, we use `emchain` and `epchain` to reproduce the event files from MOS and pn CCDs. The flares are filtered out with `mos-filter` and `pn-filter`. The point sources are detected by `cheese`.

We apply the `mos-spectra` and `pn-spectra` to create spectra and images. The instrumental background is modeled with routines `mos_back` and `pn_back`, which use data from the unexposed pixels in the detector corner, and filter-wheel closed data sets with hardness ratios and count rates similar to those measured during the observations.

The MOS1, MOS2, and pn images are combined with the `comb`, then we use the routine `adapt` to create the quiescent instrumental background subtracted, exposure corrected EPIC images, which are binned by a factor of 2 and adaptively smoothed with a minimum number of 100 counts bin^{-1} .

Similarly, we use the HEASARC X-ray Background Tool to extract an off-cluster RASS sky background spectrum, which is also fitted with the 3-component model. Then the quiescent instrumental background-subtracted MOS1, MOS2 and pn on- and

RASS off-cluster spectra are jointly fitted. However, here we need to include additional model components for the residual instrumental and/or variable sky background: 1) gaussian emission lines to account for a few strong instrumental lines and for possible solar wind charge exchange contributions to the OVII and OVIII $K\alpha$ lines and 2) a `power-law` not folded through the instrumental effective areas for residual soft proton contamination (Kuntz & Snowden 2008).

3 RESULTS

We here describe the general X-ray morphological and spectral properties of the clusters, while their individual multiwavelength characteristics will be detailed in § 4.1.

3.1 Morphological Structure

Fig. 1 presents the X-ray images of the cluster/QSO pair fields. The large fields of view shown in the left panels include the UV-bright background QSOs, which are also luminous in X-ray and are marked with cyan circles. The right panels show the multiwavelength close-ups of the clusters, including the diffuse X-ray emission intensity maps with detected discrete sources excised, as well as optical images and radio continuum contours. Each field contains one known cluster, except for A959, which is accompanied by a small group at its west-southwest (WSW) direction. A more quantitative discussion of these X-ray morphology will be given in § 4.2.

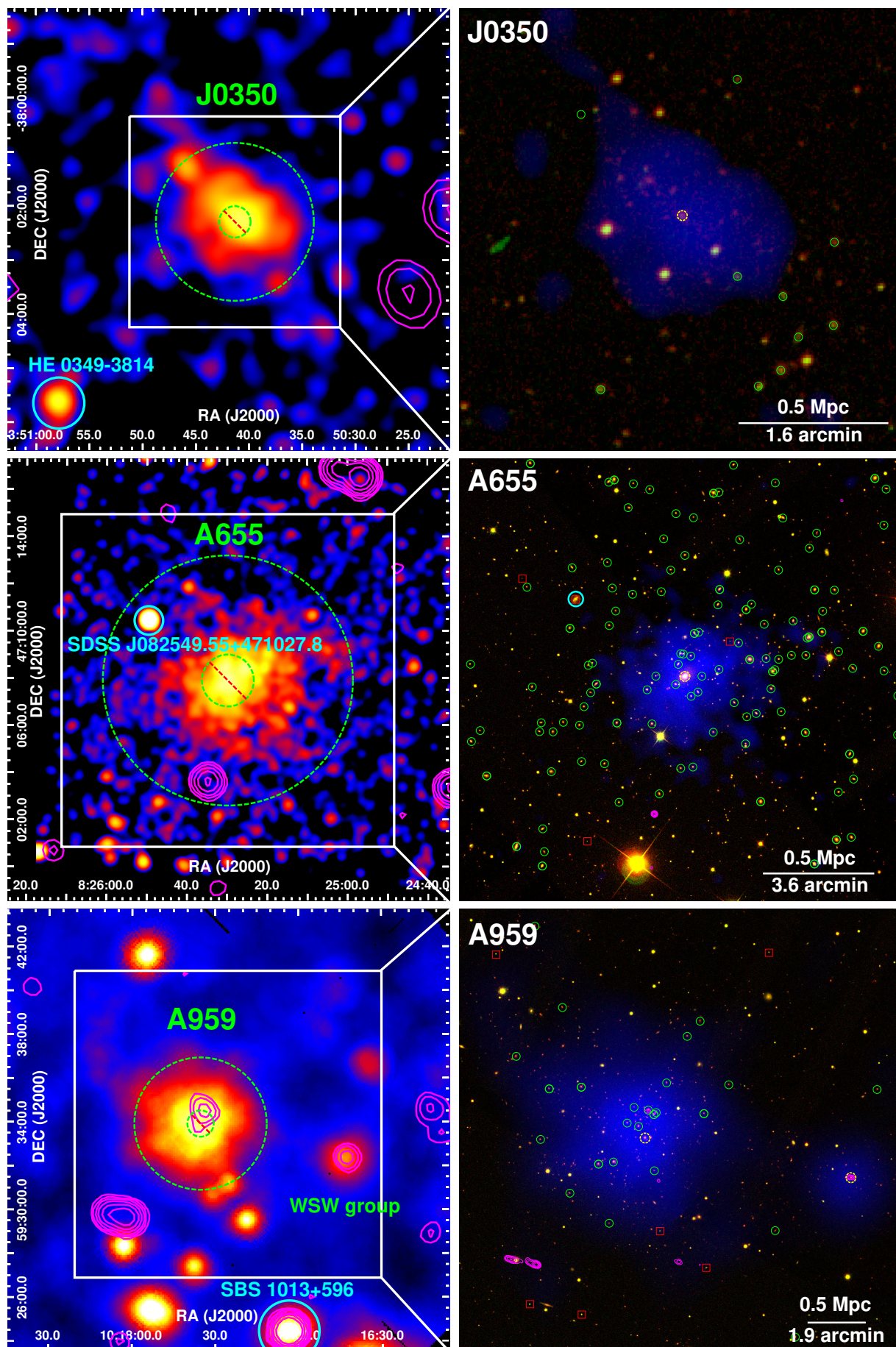
The upper panels of Fig. 2 presents the radial intensity profile of the diffuse X-ray emission. These profiles are constructed around the X-ray peaks of individual clusters and are fitted with the standard β -model (Cavaliere & Fusco-Femiano 1976) of the form:

$$I = I_0(1 + x^2)^{1/2 - 3\beta}, \quad (1)$$

where $x = R/r_c$, while I_0 , r_c , and β are the free parameters. Their best-fitting values are included in Table 2. The profiles reach out to r_{500} , except for A655 due to its relatively shallow data. The β value is consistent with the results of Sanderson et al. (2003), who find β is close to canonical value of $2/3$ for hot ($> 3 - 4$ keV) clusters and becomes increasing flattened below this temperature. We use the fit result to estimate the central gas density and M_{gas} within r_{500} in § 4.3.3.

3.2 Thermal Properties

The cluster emission is fitted with the XSPEC (version 12.8.0; Arnaud 1996) package and the AtomDB (version 2.0.1) database of atomic data. We use `apec` emissivity model to fit the on-cluster emission, with the model metallicity fixed to 0.3 solar (Asplund et al. 2009) and redshift fixed to the optical redshift of BCG. We also apply the Tuebingen-Boulder absorption model (`tbabs`) for X-ray absorption by the interstellar medium (ISM), with the hydrogen column density N_H fixed to the Galactic value from the `NHtot` tool (Willingale et al. 2013). The spectroscopic X-ray temperature is measured in 0.15–0.75 r_{500} (marked as dashed annuli in the left panels of Fig. 1), the inner boundary of 0.15 r_{500} is chosen to exclude most of the possible cool core (CC) region with a large dispersion in observation, while the outer boundary of 0.75 r_{500} is limited by the quality of the spectroscopic data. The r_{500} is estimated iteratively from $M - T$ relation (Sun et al. 2009 for *Chandra*



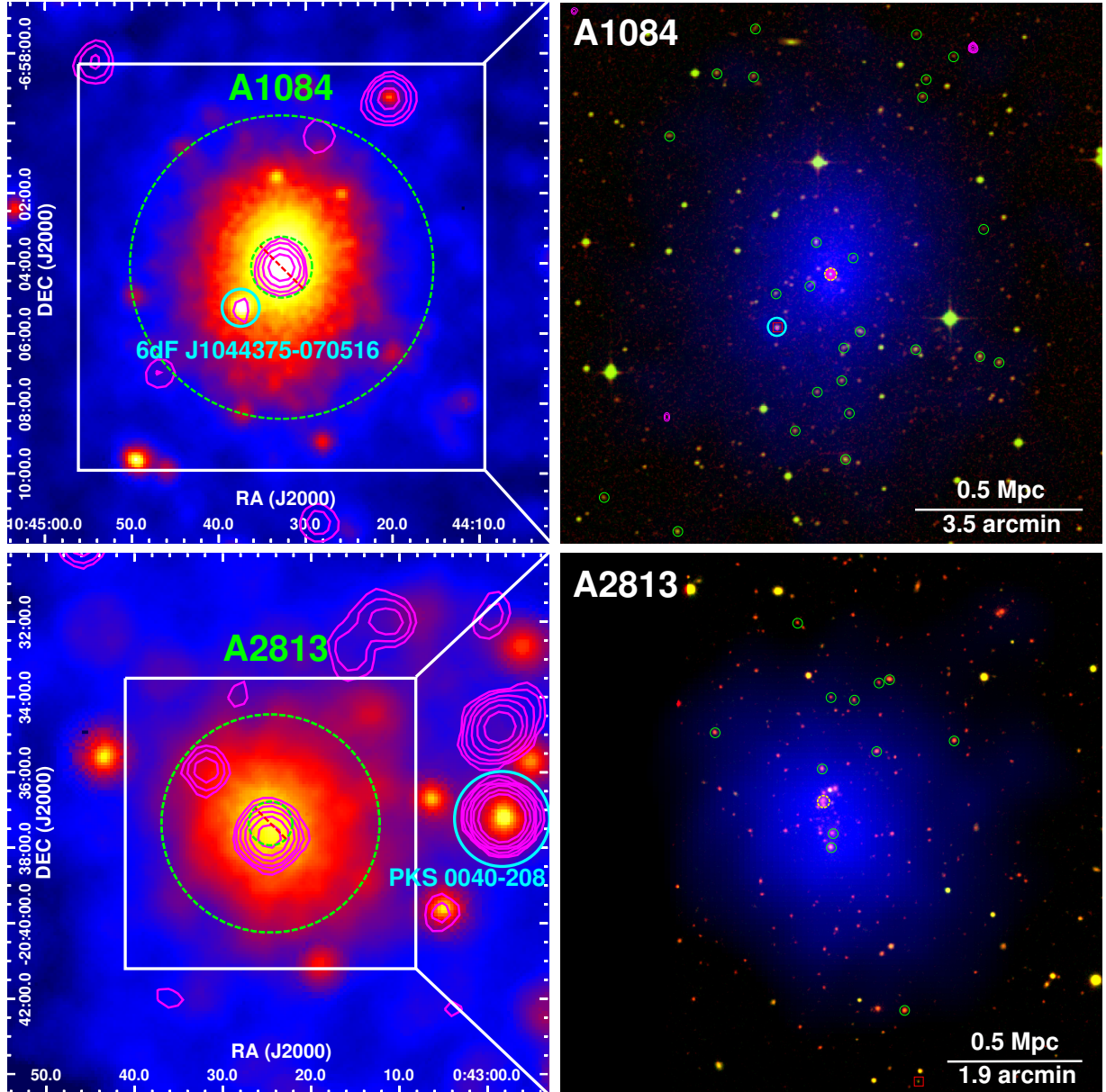


Figure 1. *Left:* *Chandra/XMM-Newton* 0.5–2 keV background subtracted, exposure corrected, and smoothed image, overlaid with 1.4 GHz continuum magenta contours from NVSS at 2, 4, 8, 16, 32, and 64 mJy beam⁻¹. The UV-bright QSO is marked as a cyan circle and labeled. The white box outlines a close-up region, and the dashed annulus is the 0.15–0.75 r_{500} region for global temperature evaluation. *Right:* a close-up multiwavelength montage: SDSS r-band (red), SDSS g-band (green), and diffuse 0.5–2 keV emission with point sources excluded (blue); DSS red band (red), DSS blue band (green) for J0350 and A1084. Galaxies (solid green circles), BCGs (dashed yellow circles), and QSOs (red boxes, UV-bright ones are marked with additional cyan circle) are labeled. The galaxy location are from SDSS (galaxy redshift within 0.01 of BCG from spectroscopic database and 0.03 from photometric database for A655, A959, and A2813) or NED (J0350 and A1084). Overlaid magenta contours represent the 1.4 GHz continuum intensity at 1, 2, 4, 8, 16, and 32 mJy beam⁻¹ from the FIRST survey (except for J0350 and A2813).

calibration and Arnaud et al. 2007 for *XMM-Newton* calibration). Table 2 includes the results of our spectral characterization of the hot ICM in the individual clusters. The single-temperature plasma model gives acceptable fits to all of them.

We also produce the radial temperature profiles of these clusters in the bottom panels of Fig. 2. Only A1084 shows a strong temperature drop toward the center when considering the error bars in temperature, which indicates that A1084 is a strong CC cluster.

4 DISCUSSION

4.1 Comparison with existing multiwavelength observations

We here present a brief comparison of the above X-ray results with the existing multiwavelength observations, focusing on the properties relevant to the dynamical states (more detailed in § 4.2) of the individual clusters. The right panels of Fig. 1 show the optical image: SDSS for A655, A959, and A2813; DSS for J0350 and A1084. We also show the radio intensity contours from the NRAO VLA Sky Survey (NVSS; Condon et al. 1998) in the left panels of

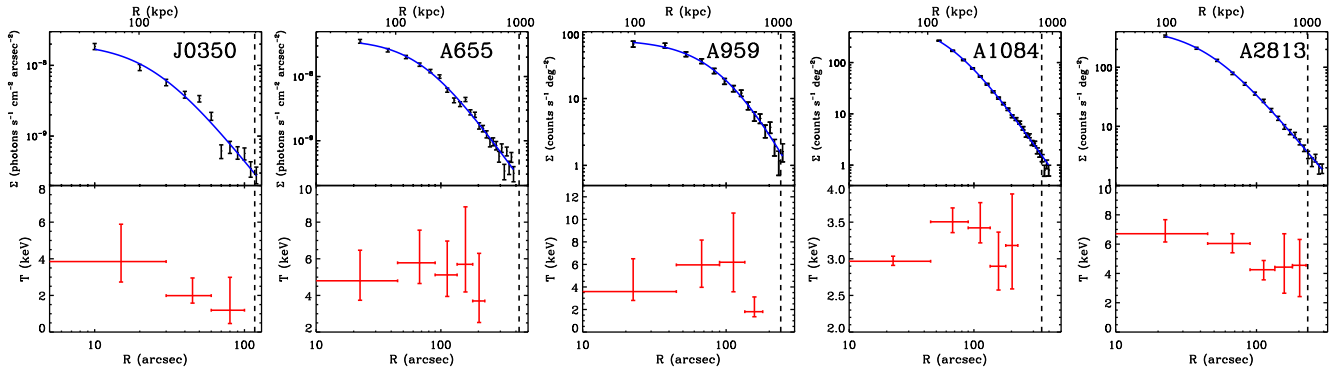


Figure 2. *Top panels:* Radial intensity profiles of the diffuse 0.5–2 keV emission for our sample clusters, together with the respective best-fitting β -models. The dashed line shows the location of r_{500} . *Bottom panels:* Radial temperature profiles of the clusters.

Table 2. Properties of galaxy clusters

Name	J0350	A655	A959	A1084	A2813
Redshift	0.363	0.129	0.288	0.133	0.292
X-ray peak position	$3^{\text{h}}50^{\text{m}}40.8^{\text{s}}, -38^{\circ}02'14''$	$8^{\text{h}}25^{\text{m}}29.8^{\text{s}}, +47^{\circ}07'57''$	$10^{\text{h}}17^{\text{m}}35.8^{\text{s}}, +59^{\circ}34'03''$	$10^{\text{h}}44^{\text{m}}33.1^{\text{s}}, -7^{\circ}04'11''$	$0^{\text{h}}43^{\text{m}}24.6^{\text{s}}, -20^{\circ}37'27''$
BCG position	$3^{\text{h}}50^{\text{m}}41.3^{\text{s}}, -38^{\circ}02'09''$	$8^{\text{h}}25^{\text{m}}29.1^{\text{s}}, +47^{\circ}08'01''$	$10^{\text{h}}17^{\text{m}}34.3^{\text{s}}, +59^{\circ}33'40''$	$10^{\text{h}}44^{\text{m}}32.9^{\text{s}}, -7^{\circ}04'08''$	$0^{\text{h}}43^{\text{m}}25.1^{\text{s}}, -20^{\circ}37'02''$
Offset (kpc)	38.4	18.7	112.6	12.6	88.7
Temperature (keV)	$2.16^{+0.82}_{-0.41}$	$4.25^{+0.84}_{-0.54}$	$5.87^{+0.80}_{-1.33}$	$3.31^{+0.12}_{-0.13}$	$5.55^{+0.99}_{-0.44}$
f_x or CR	0.79	9.68	0.12	0.41	0.24
η (10^{-4})	3.5	39.1	16.7	49.8	34.9
$\chi^2_T/d.o.f.$	22/23	114/111	306/300	1603/1631	766/849
M_{500} ($10^{14} M_{\odot}$)	$0.87^{+0.55}_{-0.28}$	$3.00^{+1.00}_{-0.65}$	$4.36^{+1.03}_{-1.70}$	$1.78^{+0.14}_{-0.15}$	$3.96^{+1.22}_{-0.56}$
r_{500} (Mpc)	$0.59^{+0.12}_{-0.06}$	$0.98^{+0.11}_{-0.07}$	$1.04^{+0.08}_{-0.14}$	$0.82^{+0.02}_{-0.02}$	$1.01^{+0.10}_{-0.05}$
I_0	$2.1^{+0.6}_{-0.4}$	$3.8^{+0.4}_{-0.3}$	$76.3^{+9.7}_{-8.6}$	$670.4^{+67.5}_{-57.3}$	$465.7^{+43.4}_{-38.8}$
r_c (Mpc)	$0.12^{+0.04}_{-0.03}$	$0.16^{+0.02}_{-0.02}$	$0.43^{+0.11}_{-0.08}$	$0.15^{+0.01}_{-0.01}$	$0.19^{+0.02}_{-0.02}$
β	$0.62^{+0.09}_{-0.06}$	$0.62^{+0.03}_{-0.03}$	$0.85^{+0.18}_{-0.12}$	$0.75^{+0.02}_{-0.02}$	$0.65^{+0.02}_{-0.02}$
$\chi^2_{\beta}/d.o.f.$	27.3/9	47.6/22	7.5/13	19.0/21	6.7/16
n_0 (10^{-3} cm^{-3})	$2.54^{+0.10}_{-0.11}$	$2.87^{+0.11}_{-0.12}$	$1.46^{+0.05}_{-0.05}$	$6.60^{+0.23}_{-0.26}$	$4.92^{+0.18}_{-0.20}$
M_{gas} ($10^{13} M_{\odot}$)	$0.80^{+0.14}_{-0.12}$	$2.73^{+0.58}_{-0.48}$	$4.32^{+0.51}_{-0.46}$	$2.68^{+0.65}_{-0.52}$	$5.91^{+1.17}_{-0.98}$
M_{star} ($10^{12} M_{\odot}$)	2.98	5.67	6.88	4.32	6.55
D_{QSO} (Mpc)	1.45	0.58	2.68	0.23	1.61
N_p (10^{20} cm^{-2})	$4.3^{+3.5}_{-1.8}$	$15.9^{+7.3}_{-4.6}$	$2.7^{+2.0}_{-1.1}$	$36.9^{+9.9}_{-7.2}$	$12.6^{+9.0}_{-5.0}$

Note. Errors are at the 90% confidence level. The offset is the projected distance between the X-ray peak and the BCG. The photon flux f_x (10^{-4} photons $\text{s}^{-1} \text{ cm}^{-2}$) for *Chandra* data or count rate CR (count s^{-1}) for *XMM-Newton* data, and η is *apex* normalization, as well as the temperature, are from the best-fitting *apex* model of each cluster. The cluster mass M_{500} and radius r_{500} are estimated from the $M - T$ relation (Sun et al. 2009 for *Chandra* calibration and Arnaud et al. 2007 for *XMM-Newton* calibration). The β -model parameters of Eq. (1) are from the best fit to the 0.5–2 keV intensity profile, the I_0 is in the unit of 10^{-8} photons $\text{s}^{-1} \text{ cm}^{-2} \text{ arcsec}^{-2}$ for *Chandra* data or count $\text{s}^{-1} \text{ deg}^{-2}$ for *XMM-Newton* data. The inferred parameters include the central proton (hydrogen) density (n_0), the hot gas mass (M_{gas}) and stellar mass (M_{star}) within r_{500} , the stellar mass is estimated with the relation of (Gonzalez et al. 2013). The proton column density (N_p) is at the projected distance (D_{QSO}) of the corresponding UV-bright background QSO.

Fig. 1 and those from the Faint Images of the Radio Sky at Twenty-cm (FIRST; Becker et al. 1995) in the right panels, except for J0350 and A2813, which are not covered by FIRST. We next discuss some notable features for the individual cluster.

J0350. Data in other bands are not notable for this cluster, although we notice a filament-like structure in the NE of cluster from the X-ray image.

A655. It is classified as a BM I-type (Bautz & Morgan 1970) cluster for its dominant cD galaxy. It does not host any significant diffuse radio emission (Rudnick & Lemmerman 2009). The large core radius (~ 1300 kpc; Strazzullo et al. 2005) from a β -model fitting of member galaxy distribution may indicate it as a disturbed cluster, because merging events could have erased the original cusp profile.

A959. This cluster has been studied extensively. Most notable are the mapping of gravitational mass via weak gravitational lensing observations (Dahle et al. 2003) and the optical spectroscopy for individual galaxies (Boschin et al. 2009). In these studies, *ROSAT* X-ray images are used for comparison. The *XMM-Newton* observation presented here allows for a refined X-ray view and multiwavelength comparison of the cluster.

There is no dominant galaxy at the cluster center. Instead, it contains several early-type galaxies of comparable brightnesses. The gravitational mass distribution shows multiple peaks or filamentary structures around the X-ray centroid of the cluster (Dahle et al. 2003). However, these peaks are well separated and are not well traced by the projected spatial distribution of galaxies, which seems to be rather structured (e.g., see Fig. 13 in Boschin et al.

2009). Such multiple-component structure is also seen in the velocity distribution of the cluster galaxies (Boschin et al. 2009).

On even larger scales, one finds the so-called WSW galaxy group, $\sim 6'$ west (slightly to the south) of A959. This group is first detected via the gravitational lensing (Dahle et al. 2003) and also in the *ROSAT* image and galaxy concentration (Boschin et al. 2009). Based on a diffuse X-ray spectrum extracted from the *XMM-Newton* observation, we find that the temperature of the plasma in the group is $T = 1.7_{-0.4}^{+2.3}$ keV, indicating $M_{200} = 0.7_{-0.3}^{+1.7} \times 10^{14} M_{\odot}$. The BCG (SDSS J101642.79+593223.3; $z=0.285$) of the group has a radio counterpart detected in both FIRST and NVSS. The redshift of the group is consistent with that of A959. These two systems appear to be gravitationally bound, because their combined gravitational mass is greater than $2.6 \times 10^{14} M_{\odot}$, required, according to the two-body model (Beers et al. 1982). Further away from A959 (beyond the *XMM-Newton* field explored here), there are two more clusters at comparable redshifts: MaxBCG J153.93477+59.57870 at $z \sim 0.281$ (Koester et al. 2007), $\sim 13'$ west, and MaxBCG J154.78308+59.76784 at $z \sim 0.284$, $\sim 18'$ NE (see Fig. 14 in Boschin et al. 2009). Therefore, A959 is apparently in a quite rich environment of the large-scale structure (Boschin et al. 2009).

A1084. Its BCG (NVSS J104432-070407) is a radio source ($F_{1.4\text{GHz}} = 31.6$ mJy; Magliocchetti & Brüggén 2007) and hosts a significant star formation ($\text{SFR} \sim 0.4 M_{\odot} \text{ yr}^{-1}$; Donahue et al. 2010), which are consistent with the fact that a CC cluster (Fig. 2) is more likely to host a BCG with star forming and/or radio emission (e.g., Donahue et al. 2010, Kale et al. 2015).

A2813. The BCG of this cluster does not show enhanced UV and mid-IR emission (Hoffer et al. 2012), which is consistent with its non-cool core (NCC) nature (Fig. 2). There is a NW extension inferred from the X-ray image, probably due to an accretion of a filament (Finoguenov et al. 2005).

4.2 Dynamical states of the clusters

Galaxy clusters are assembled via mergers of hierarchical systems, ranging from the IGM to sub-clusters of galaxies at the intersections of cosmic web filaments. Therefore, depending on its recent merger history, a cluster can be in quite different dynamical states.

Because of the diversity in the recent merger histories of individual clusters, which is further complicated by their projection effects, their dynamical states are not straight-forward to determine. In Appendix A, we present a review of various dynamical state diagnostics based on X-ray morphological properties of clusters. The criteria for a relaxed cluster is the power ratio P_3/P_0 (Buote & Tsai 1995), centroid shift w (Mohr et al. 1993), surface brightness concentration c_{SB} (Santos et al. 2008), photon asymmetry A_{phot} (Nurgaliev et al. 2013), and symmetry-peakiness-alignment SPA (Mantz et al. 2015). The results of the applications of these diagnostics to our sample clusters are listed in Table 3.

We have also considered other cluster dynamical state tracers. Clusters can be categorized into CC clusters and NCC clusters (e.g., Jones & Forman 1984; Sanderson et al. 2006). A CC cluster tends to show a relaxed and symmetric morphology, whereas an NCC cluster likely exhibits a disturbed overall shape and substructure. We consider the presence of a central temperature drop as the evidence for a CC from Fig. 2.

Another useful diagnostic for the dynamic state is the offset between the X-ray centroid of a cluster from its BCG. It has been shown that the BCG tends to be found positionally at the gravi-

tational center and kinematically near the rest frame of a cluster (e.g., Cui et al. 2016). Therefore, a large offset from the X-ray centroid of a cluster would indicate an ongoing or recent merger activity (Jones & Forman 1984; Lin & Mohr 2004). Previous studies show that an offset of ~ 15 kpc may be used to distinguish a relaxed cluster from an un-relaxed one (e.g., offsets of ≤ 15 kpc as relaxed clusters in Sanderson et al. 2009; offsets center at $\sim 10/\sim 50$ kpc for relaxed/un-relaxed clusters in von der Linden et al. 2014). The X-ray/BCG offsets of our sample are listed in Table 2.

We also incorporate information from observations at other wavelengths from § 4.1. Such information, though generally quite limited, may provide additional diagnostics of the cluster dynamical states.

With the above diagnostics in consideration, we make general assessments of the dynamics states of our sample clusters. We find that A1084 is a well relaxed cluster, which is the only one that passes all the criteria (morphological parameters; CC cluster; small X-ray/BCG offset; BCG hosts SF and AGN activities). Other clusters all show multiple indications for major disturbance, although each of them may meet at least one of the morphological parameters for a relaxed state. Their X-ray/BCG offsets are larger than 15 kpc, their temperature profiles do not show a strong center drop, consistent with their disturbed dynamical states. This diversity in the apparent dynamical states reflects the complexity of cluster evolution and potentially the project effects, which limits the usefulness of any single diagnostic indicator.

4.3 Baryon contents

Here we first estimate for each cluster the masses of the three main cluster components: dark matter, ICM, and stars. We will then compare the total baryon budgets with the values expected from the standard cosmology.

4.3.1 Total gravitational mass

We use the $M - T$ relation (Sun et al. 2009 for *Chandra*; Arnaud et al. 2007 for *XMM-Newton*) to estimate the total cluster mass M_{500} in r_{500} , as the X-ray temperature is a quite robust mass proxy. However, this X-ray hydrostatic mass could be underestimated because of additional non-thermal pressure from e.g., gas bulk motion and turbulence (e.g., Nagai et al. 2007; Mahdavi et al. 2008; Lau et al. 2009). Assuming a typical 15% hydrostatic bias (X-ray hydrostatic mass is 15% lower than the true cluster mass) in total cluster mass induces to 21% in M_{500} (Rozo et al. 2014). Moreover, most clusters in our sample are unrelaxed clusters, thus the hydrostatic bias could be even higher.

We note there are some cross-calibration issues between *Chandra* and *XMM-Newton*, especially the temperature from *Chandra* are systematically higher than *XMM-Newton* (e.g., Schellenberger et al. 2015). We use the temperature relation of ACIS and combined *XMM-Newton* in the full band in Schellenberger et al. (2015) to rescale the temperature of *Chandra* to *XMM-Newton*, and then re-estimate the M_{500} based on the *XMM-Newton* $M - T$ relation, the mass difference is within 30%. However, our final results remain unchanged when including the above bias.

4.3.2 Hot ICM mass

For the hot ICM, we calculate the central de-projected proton (or hydrogen) density distribution from our β -model fit to the ra-

Table 3. X-ray morphological parameters

Name (1)	$P_3/P_0 \times 10^{-7}$ (2)	$w \times 10^{-2}$ (3)	c_{SB} (4)	A_{phot} (5)	SPA (6)
J0350	$9.56^{+19.62}_{-8.51}$	$1.36^{+1.23}_{-0.70}$	$0.070^{+0.030}_{-0.026}$	$0.09^{+0.02}_{-0.06}$	0.813 –1.582 0.923
A655	$1.16^{+1.74}_{-0.97}$	$1.69^{+0.66}_{-0.65}$	$0.045^{+0.006}_{-0.007}$	$0.06^{+0.01}_{-0.02}$	0.533 ± 0.171 – 1.298 ± 0.413 0.631 ± 0.255
A959	$2.54^{+4.28}_{-2.09}$	$1.37^{+0.84}_{-0.62}$	$0.013^{+0.004}_{-0.004}$	$0.48^{+0.24}_{-0.43}$	0.876 ± 0.152 – 1.961 ± 0.389 1.346 ± 0.241
A1084	$0.27^{+0.16}_{-0.10}$	$0.31^{+0.02}_{-0.02}$	$0.164^{+0.003}_{-0.002}$	$0.14^{+0.01}_{-0.01}$	1.158 ± 0.029 – 0.814 ± 0.008 1.356 ± 0.034
A2813	$0.41^{+0.75}_{-0.28}$	$1.33^{+0.14}_{-0.15}$	$0.040^{+0.003}_{-0.003}$	$0.05^{+0.02}_{-0.03}$	1.112 ± 0.081 – 1.040 ± 0.007 1.193 ± 0.058

Note. (1) cluster name. (2) Power ratio. (3) Centroid shift. (4) Surface brightness concentration. (5) Photon asymmetry. (6) Symmetry-Peakiness-Alignment. More details in Appendix A.

dial intensity profile (e.g., Sarazin 1988), under assumptions of the spherical symmetry and isothermal temperature distribution (the cluster emissivity function in soft 0.5-2 keV band is sensitive to density but almost insensitive to temperature at $T > 2$ keV),

$$n_H = n_0 \left(1 + \frac{r^2}{r_c^2}\right)^{-\frac{3}{2}\beta}. \quad (2)$$

We adopt the equation (10) of Ge et al. (2016) to estimate n_0 :

$$n_0 = \frac{180}{\pi} \sqrt{\frac{10^{14} 4 \sqrt{\pi} I_0 \Gamma(3\beta)}{\left(\frac{n_e}{n_H}\right) \frac{CR}{\eta} r_c \Gamma(3\beta - 1/2)}} \quad (\text{XMM-Newton data}), \quad (3)$$

$$n_0 = \frac{3600 \times 180}{\pi} \sqrt{\frac{10^{14} 4 \sqrt{\pi} I_0 \Gamma(3\beta)}{\left(\frac{n_e}{n_H}\right) \frac{f_x}{\eta} r_c \Gamma(3\beta - 1/2)}} \quad (\text{Chandra data}). \quad (4)$$

These equations use the parameters from the β -model fit (I_0 , β , r_c in a unit of cm) of the exposure-corrected intensity image, and the spectral dependent conversion from the emission measure to the count rate ($\frac{CR}{\eta}$ or $\frac{f_x}{\eta}$) with the on-axis response files of each observation. This is different from the method used in such works as Mohr et al. (1999) and Ettori et al. (2004), which integrate the temperature-dependent electron density along the line of sight within a somewhat artificial cluster ‘‘boundary’’, where the X-ray emission is insignificant. In contrast, our analytical formula accounts for all the X-ray emission along the line of sight. The n_0 and the hot ICM mass (M_{gas}) within r_{500} are listed in Table 2.

The systematic error of M_{gas} is dominated by the uncertainty from integration gas distribution in the outer radius, which is closely related to the β value. The β varies with cluster mass (e.g., Sun et al. 2009) and radius (e.g., Morandi et al. 2015). We assume a typical 10% uncertainty in β to estimate the error in M_{gas} . Moreover, the gas mass could be overestimated due to bias of gas clumping, though it should be small within r_{500} .

For future comparison, Table 2 also lists the estimation of the hot ICM proton column density at the projected distances of the QSO for each cluster as

$$N_p = \sqrt{\pi} n_0 r_c \frac{\Gamma(3\beta/2 - 1/2)}{\Gamma(3\beta/2)} (1 + x^2)^{1/2 - 3\beta/2} \quad (\beta > 1/3). \quad (5)$$

4.3.3 Warm-hot ICM

The larger goal of the work presented herein and in our previous publications (Wang & Walker 2014; Ge et al. 2016; Burchett et al. 2018) is to leverage diagnostics of both the hot ($T > 10^6$ K) and warm-hot ($T = 10^{5-6}$ K) gas afforded by X-ray imaging/spectroscopy and UV absorption lines, respectively, to characterize the ICM in its baryon budget and impact on the circumgalactic media of cluster galaxies. We now present an analysis of

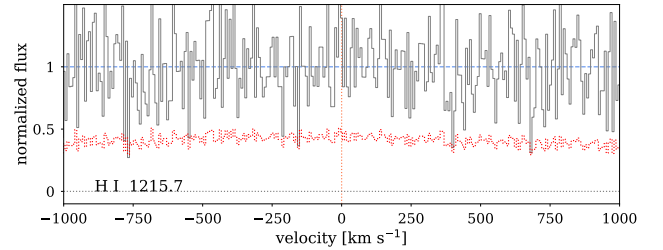


Figure 3. Continuum-normalized spectrum of SBS 1013+596 in the region where H I Ly α would fall at the redshift of A959, to which the velocity scale is relative. The error vector is shown red. While the spectrum is quite noisy, we do not detect any statistically significant Ly α features within ± 1000 km s $^{-1}$ of the cluster redshift.

the existing HST/COS spectrum of SBS 1013+596, whose sightline probes the outskirts of A959 at an impact parameter of 2.68 Mpc, or 2.58 r_{500} . Our analysis follows closely that of Burchett et al. (2018, Section 4.2). The SBS 1013+596 spectrum was obtained in HST programme GO 12593 (PI: Nestor) using the COS G160M grating, covering the wavelength range of 1410-1774 Å with an average S/N of 2.4 in the region of interest (near the observed wavelength of the H I Ly α line at $z = 0.288$). Due to the wavelength coverage of the G160M grating, H I Ly β and the O VI are not accessible. Fig. 3 shows the QSO spectral region within ± 1000 km s $^{-1}$ of the Ly α observed wavelength at the redshift of A959.

We report no statistically significant detections of H I Ly α near the redshift of A959, possibly due in part to the low S/N of the archival SBS 1013+596 spectrum. However, we proceed with the analysis detailed by Burchett et al. (2018) to place constraints on the physical conditions and total column density of the 10^{5-6} K gas. Briefly, the analysis premise is as follows: assuming thermal broadening of any potential Ly α lines, we generate numerous realizations of Voigt profiles on a grid of Doppler b -parameters and column densities ($N(\text{H I})$). We then convolve these synthetic profiles with the instrumental line spread function and inject them into a flat spectrum with S/N commensurate with that of the actual data. Finally, measuring the equivalent widths and associated uncertainties of these profile realizations enable us to quantify their detection significance. Fig. 4 shows the matrix of detection significance for the range of $N(\text{H I})$ and b , where the colors indicate the detection significance according to the values shown on the colorbar. We encourage the reader to contrast Fig. 4 to its counterpart in Burchett et al. (2018, Fig. 10), as the quantitative difference in data quality between those targeted, S/N ~ 18 spectra and the archival spectrum analysed here is clearly seen. The Burchett et al. (2018) data

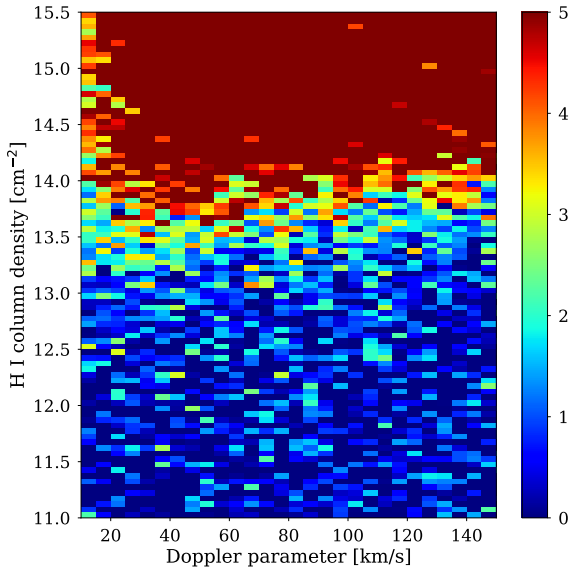


Figure 4. Detection significance (see colorbar on the right) of synthetic H I Ly α features at the redshift of A959 as a function of H I column density and Doppler b value. Assuming the lines are thermally broadened, one may associate these b values to gas temperature. Note that while lines become more difficult to detect with increasing b , with the column density limits increasing by 0.5 dex over the range of Doppler parameter, the poor S/N of this archival spectrum hardly enable detecting lines of $N(\text{H I}) < 13.5 \text{ cm}^{-2}$ for even narrow Ly α lines.

enabled sensitivity to column densities approximately an order of magnitude lower than in the present work ($N(\text{H I}) \sim 10^{12.5} \text{ cm}^{-2}$ vs. $\sim 10^{13.5} \text{ cm}^{-2}$ for $b = 40 \text{ km s}^{-1}$ lines). Given that the $b \sim 70 \text{ km s}^{-1}$ broad Ly α lines associated with A1926 reported by Burchett et al. (2018) had $N(\text{H I}) < 10^{13.7} \text{ cm}^{-2}$, only the strongest component would be possibly (but unlikely) detected, and the remaining two $N(\text{H I}) \sim 10^{13.1} \text{ cm}^{-2}$ lines would surely be lost in the noise. Recall that two out of three of the Burchett et al. (2018) sightlines were targeted with appropriate S/N to robustly detect such features and probe X-ray bright galaxy clusters at interesting impact parameters; the third is among the highest S/N QSO spectra ever recorded by HST/COS. We emphasize that chance alignments alone between massive clusters and QSO sightlines that have been observed with sufficient data quality in the HST archive are simply insufficient to build samples and conduct the analysis necessary to study the warm-hot gas contribution to cluster baryon budgets.

Finally, we convert the detection statistics as functions of b value and column density to total H column density ($N(\text{H})$) to compare with the constraints from X-rays. As in Burchett et al. (2018), we use the Oppenheimer & Schaye (2013) ionization models to obtain the ionization fractions H^o/H as a function of temperature (obtained from the Doppler b values). The $N(\text{H})$ is then the measured $N(\text{H I})$ divided by the ion fraction. Fig. 5 shows the results, comparing the limits we are able to place on A959 with the constraints Burchett et al. (2018) placed on A1095. Here, the solid line shows the $3\text{-}\sigma$ detection threshold as a function of temperature, and the shaded regions below these lines represent the amount of the $N(\text{H})$ that could be ‘hidden’ in the noise of the data. The markers with error bars represent the individual components of broad

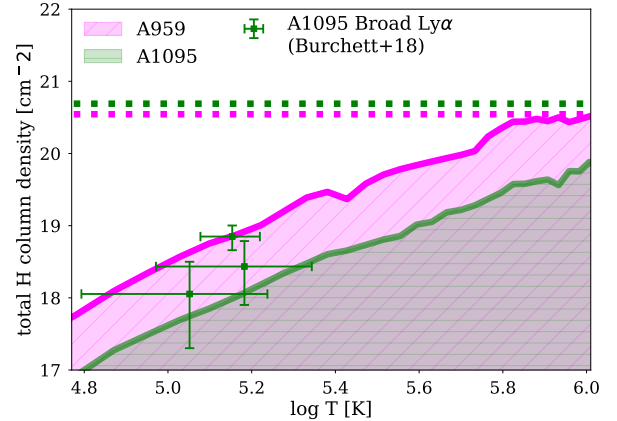


Figure 5. Limits on the total H column density from gas in the warm-hot gas phase as a function of temperature under thermal line broadening (solid lines and shaded regions) relative to that from X-ray measurements of the $> 10^6 \text{ K}$ phase (dotted horizontal lines). Measurements corresponding to A959/SBS 1013+596 are colored purple, and we show the limits and measurements derived for A1095 (Burchett et al. 2018) in green for comparison. In this representation, the QSO spectra enable detecting $N(\text{H})$ values above the solid lines, and $N(\text{H})$ values lying in the shaded regions would be obscured by the noise in the data. Note that the three previously detected components associated with A1095 would be undetectable in A959 given the S/N of the existing spectrum. In A959, the amount of total H column hidden in $10^{5.8} \text{ K}$ gas could equal that in the hot X-ray traced material.

Ly α associated with A1095. Clearly, these components would be missed in spectra with similar S/N to that of SBS 1013+596 analyzed here. We suggest that these data serve as a useful guide to establish observational strategies in pursuing these simultaneous hot/warm-hot constraints with a targeted sample of the cluster/QSO sightline pairs.

4.3.4 Baryon fraction of the clusters

Fig. 6 shows the total baryon fraction over the total gravitational mass of the hot ICM and stars. The stellar mass is estimated with the scaling relation of $M_{*,3D} = 3.2 \times 10^{-2} (M_{500}/10^{14} M_{\odot})^{0.52}$ from Gonzalez et al. (2013), whose estimate includes the additional contribution from intracluster stars (ICS) and correction for the completeness from fainter galaxies as well as the projection from galaxies outside r_{500} in the line of sight direction. The stellar fractions of the individual cluster are also presented in Fig. 6. Though there are some systematic biases when determining stellar mass, e.g., initial mass function (IMF) variation (radial and galaxy dependent); ICS contribution; uncertainty in mass-to-light ratio depending on different models and methods; uncertainty in the faint end slope of the galaxy luminosity function; and deprojection of galaxy distribution from 2D to 3D (e.g., Gonzalez et al. 2013; Budzynski et al. 2014; Kravtsov et al. 2018). The scatter of the stellar mass is at a level of 30% (Lin & Mohr 2004; Kravtsov et al. 2018). Thus the biases in stellar mass estimation have a minor impact to our total baryon fraction, because the dominant baryon component is in hot gas for our cluster sample.

For comparison, Fig. 6 further includes results from our previous studies of four clusters (Ge et al. 2016), which are all disturbed clusters. We account for the 21% hydrostatic bias in M_{500} as dis-

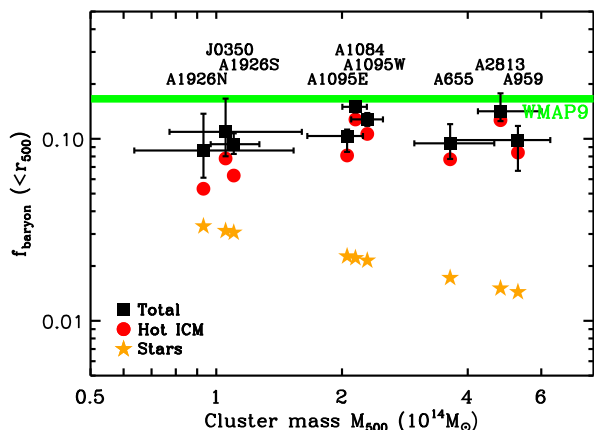


Figure 6. Baryon fraction within r_{500} as a function of M_{500} : dots are the hot ICM fractions; stars represent the stellar mass fractions estimated based on the scaling relation of [Gonzalez et al. \(2013\)](#), which includes the additional contribution from ICS; boxes are the total baryon fractions of hot ICM plus stars. The green band marks the uncertain range of the WMAP 9-year baryon fraction ([Hinshaw et al. 2013](#)). The above labels are names of corresponding clusters. We also include four clusters in [Ge et al. \(2016\)](#).

cussed in § 4.3.1. As the M_{500} increasing, the r_{500} for estimating M_{gas} and M_{star} also increases. However, the f_{gas} , which dominates the baryon budget, only increase 2.6% with $f_{gas} \sim M_{500}^{0.135}$ ([Sun et al. 2009](#)), while f_{star} decreases with [Gonzalez et al. \(2013\)](#) relation. All the clusters show baryon deficiency compared with the cosmological fraction determined from the Wilkinson Microwave Anisotropy Probe (WMAP) 9-year data ($\sim 17\%$; [Hinshaw et al. 2013](#)).

A portion of this missing baryon matter may be ejected out of the central r_{500} regions due to energetic processes such as AGN feedback (e.g., [McCarthy et al. 2011](#)), while some fraction may reside in other gas phases, such as the warm and warm-hot ICM. As demonstrated in the previous subsection and by [Burchett et al. \(2018\)](#), high-quality, targeted QSO absorption line observations will help to characterize or constrain these missing baryons.

5 SUMMARY

We have studied a sample of X-ray-selected galaxy clusters that are paired with UV-bright background QSOs. While this study is based primarily on *Chandra* and *XMM-Newton* observations, we have also incorporated the single existing archival HST/COS spectrum for the QSO sightlines, as well as radio and optical observations for all, in the analysis of the baryon content and dynamical state of the clusters. Our major results and conclusions are as follows:

- We have characterized the X-ray morphological and spectral properties of the clusters. The radial profile of the diffuse X-ray emission can be reasonably well fitted with a β -model out to r_{500} except for A655, due to the shallow exposure. A single-temperature plasma describes well the average spectra of the clusters.
- Most of the clusters are dynamically disturbed, judging from their quantitative X-ray morphological parameters, temperature profiles, X-ray/BCG offsets, diffuse radio features, and BCG activities. These disturbances may lead to underestimation of the total gravitational masses of the clusters.
- The HST/COS spectrum allows us to place only weak constraints on the warm-hot gas content of A959. This analysis demon-

strates the need to obtain high S/N spectra of these QSOs in a focused observing programme.

- All the clusters show an evidence for missing baryons considering the hydrostatic bias. They may be located outside of the cluster regions explored here. Alternatively, they may reside in the warm and warm-hot ICM, which are yet to be discovered.

With these in consideration, targeted UV absorption line spectroscopy of the background QSOs will help us to characterize how the heating/cooling may depend on the dynamical state and mass of the cluster, as well as the impact distances, advancing our understanding of the structure formation and baryon evolution in the Universe.

ACKNOWLEDGEMENTS

C.G. acknowledges support from the National Natural Science Foundation of China (No. 11703090). Z.L. acknowledges support from the Recruitment Program of Global Youth Experts. Q.G. is supported by the National Key Research and Development Program of China (No. 2017YFA 0402703), and by the National Natural Science Foundation of China (No. 11733002). L.J. acknowledges support from the Joint Funds of the National Natural Science Foundation of China under grant U1531248.

APPENDIX A: DYNAMICAL STATE DIAGNOSTICS OF GALAXY CLUSTERS: X-RAY MORPHOLOGICAL PARAMETERS

Here we provide a systematical review of various diagnostics based on the X-ray morphological parameters. The used quantitative morphological indicators generally fall into two categories: (1) the bulk asymmetry, e.g., the power ratio ([Buote & Tsai 1995](#)), the centroid shifts ([Mohr et al. 1993](#)), the photon distribution asymmetry (A_{phot} , [Nurgaliev et al. 2013](#)); (2) the presence of a CC, e.g., the surface brightness concentration parameter ([Santos et al. 2008](#)). Apparently, combining the above two categories can provide a better separation of clusters at different dynamical states. An example is the symmetry-peakiness-alignment (SPA) criterion for relaxation ([Mantz et al. 2015](#)). Here, we briefly describe these morphological parameters and their relations.

The power ratio method (see details in [Buote & Tsai 1995](#); [Jeltema et al. 2005](#)) is motivated by identifying the X-ray surface brightness as a representation of the projected mass distribution of a cluster, which aims to parametrize the substructure in the ICM and to relate it to the dynamical state of a cluster. The power ratio P_3/P_0 has been found to be sensitive to asymmetries in the aperture radius (r_{500} in our case) and provides a useful measure of the dynamical state of a cluster. We use the cut of [Böhlinger et al. \(2010\)](#) to separate relaxed cluster ($P_3/P_0 \leq 1.5 \times 10^{-7}$) and disturbed cluster ($P_3/P_0 > 1.5 \times 10^{-7}$).

The centroid shift parameter w ([Mohr et al. 1993](#); [Poole et al. 2006](#)) measures the centroid variations in different aperture sizes and is defined as the standard deviation of the different center shifts (in units of r_{500}). We also use the cut of [Böhlinger et al. \(2010\)](#) to separate relaxed cluster ($w \leq 0.01$) and disturbed cluster ($w > 0.01$).

The surface brightness concentration parameter c_{SB} ([Santos et al. 2008](#)) measures the ratio of the peak over the ambient surface brightness and is very effective to distinguish CC from NCC clusters. We use three categories of ([Santos et al. 2008](#)): non-CC

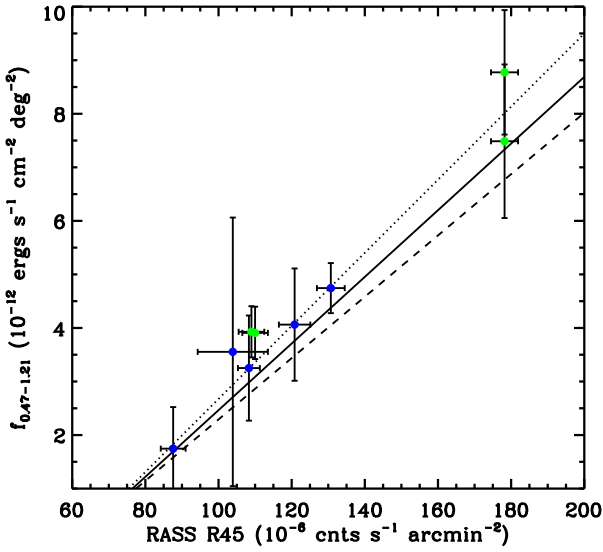


Figure A1. 0.47-1.21 keV on-cluster sky flux vs. off-cluster RASS R45 (0.47-1.21 keV) flux. Blue dots represent five clusters in the present sample, while green dots are four clusters from (Ge et al. 2016). Error bars are at the 90% confidence level. The three lines are from (Sun et al. 2009), with the expected conversions between two fluxes, assuming two thermal components for the soft sky background (all with $T_{cool} = 0.1$ keV). The solid line is for $T_{hot} = 0.25$ keV and $NORM_{hot} / NORM_{cool} = 0.5$. The dotted line is for $T_{hot} = 0.2$ keV and $NORM_{hot} / NORM_{cool} = 0.5$. The dashed line is for $T_{hot} = 0.3$ keV and $NORM_{hot} / NORM_{cool} = 1$.

($c_{SB} < 0.075$), moderate ($0.075 < c_{SB} < 0.155$), and pronounced ($c_{SB} > 0.155$) CC.

The photon distribution asymmetry parameter A_{phot} (Nurgaliev et al. 2013) measures the uniformity of the angular X-ray photon distribution in radial annuli. The parameter quantifies the deviation from the idealized axisymmetric case. We use the threshold values of Nurgaliev et al. (2013) to separate low ($A_{phot} < 0.15$), medium ($0.15 < A_{phot} < 0.6$), and strong asymmetry ($A_{phot} > 0.6$) clusters. As both A_{phot} and w measure the bulk asymmetry on intermediate scales (in r_{500}), thus they are correlated strongly (Fig. 8 in Nurgaliev et al. 2013). Furthermore, these asymmetry indicators, combined with a CC indicator such as concentration c_{SB} , show a better separation of clusters at different states of dynamical equilibrium, e.g., the asymmetry-concentration diagram (Fig. 7 in Nurgaliev et al. 2013).

The symmetry (s)-peakiness (p)-alignment (a) (Mantz et al. 2015) method classifies the cluster dynamical state based on both asymmetry and CC indicators. The p contains the information of the flux ratio in small and large apertures, and is similar to the definition of c_{SB} , thus they correlate strongly with each other (Fig. 9 in Mantz et al. 2015). The s and a have similar definitions with centroid shift, and they all measure bulk asymmetry, thus they correlate strongly with each other (Figs. 7-8 in Mantz et al. 2015). The combination of asymmetry indicators such as s and a with a CC indicator such as p separates the relaxed cluster from un-relaxed cluster well (Figs. 8,12 in Mantz et al. 2015). We use the cuts of $s > 0.87$, $p > -0.82$, and $a > 1.00$ (Mantz et al. 2015) as the criterion for a relaxed cluster.

REFERENCES

- Arnaud K. A., 1996, in Jacoby G. H., Barnes J., eds, ASP Conf. Ser. Vol. 101, Astronomical Data Analysis Software and Systems V. Astron. Soc. Pac., San Francisco, p. 17
- Arnaud, M., Pointecouteau, E., & Pratt, G. W. 2007, A&A, 474, L37
- Asplund, M., Grevesse, N., Sauval, A. J., & Scott, P. 2009, ARA&A, 47, 481
- Bautz, L. P., & Morgan, W. W. 1970, ApJ, 162, L149
- Becker, R. H., White, R. L., & Helfand, D. J. 1995, ApJ, 450, 559
- Beers, T. C., Geller, M. J., & Huchra, J. P. 1982, ApJ, 257, 23
- Böhringer, H., Schuecker, P., Pratt, G. W., et al. 2007, A&A, 469, 363
- Böhringer, H., Pratt, G. W., Arnaud, M., et al. 2010, A&A, 514, A32
- Bonamente, M., Hasler, N., Bulbul, E., et al. 2012, New Journal of Physics, 14, 025010
- Boschin, W., Barrena, R., & Girardi, M. 2009, A&A, 495, 15
- Buote, D. A., & Tsai, J. C. 1995, ApJ, 452, 522
- Budzynski, J. M., Kopusov, S. E., McCarthy, I. G., & Belokurov, V. 2014, MNRAS, 437, 1362
- Burchett, J. N., Tripp, T. M., Wang, Q. D., et al. 2018, MNRAS, 475, 2067
- Cavaliere, A., & Fusco-Femiano, R. 1976, A&A, 49, 137
- Condon, J. J., Cotton, W. D., Greisen, E. W., et al. 1998, AJ, 115, 1693
- Cui, W., Power, C., Biffi, V., et al. 2016, MNRAS, 456, 2566
- Dahle, H., Pedersen, K., Lilje, P. B., Maddox, S. J., & Kaiser, N. 2003, ApJ, 591, 662
- Donahue, M., Bruch, S., Wang, E., et al. 2010, ApJ, 715, 881
- Eckert, D., Vazza, F., Ettori, S., et al. 2012, A&A, 541, A57
- Emerick, A., Bryan, G., & Putman, M. E. 2015, MNRAS, 453, 4051
- Ettori, S., Tozzi, P., Borgani, S., & Rosati, P. 2004, A&A, 417, 13
- Finoguenov, A., Böhringer, H., & Zhang, Y.-Y. 2005, A&A, 442, 827
- Ge, C., Wang, Q. D., Tripp, T. M., et al. 2016, MNRAS, 459, 366
- Gonzalez, A. H., Sivanandam, S., Zabludoff, A. I., & Zaritsky, D. 2013, ApJ, 778, 14
- Hickox, R. C., & Markevitch, M. 2006, ApJ, 645, 95
- Hinshaw, G., Larson, D., Komatsu, E., et al. 2013, ApJS, 208, 19
- Hoffer, A. S., Donahue, M., Hicks, A., & Barthelmy, R. S. 2012, ApJS, 199, 23
- Jeltema, T. E., Canizares, C. R., Bautz, M. W., & Buote, D. A. 2005, ApJ, 624, 606
- Jones, C., & Forman, W. 1984, ApJ, 276, 38
- Kale, R., Venturi, T., Cassano, R., et al. 2015, A&A, 581, A23
- Koester, B. P., McKay, T. A., Annis, J., et al. 2007, ApJ, 660, 239
- Kravtsov, A. V., Vikhlinin, A. A., & Meshcheryakov, A. V. 2018, Astronomy Letters, 44, 8
- Kuntz, K. D., & Snowden, S. L. 2008, A&A, 478, 575
- Lau, E. T., Kravtsov, A. V., & Nagai, D. 2009, ApJ, 705, 1129
- Lin, Y.-T., & Mohr, J. J. 2004, ApJ, 617, 879
- Lu, Z., & Wang, Q. D. 2011, MNRAS, 413, 347
- Magliocchetti, M., & Brüggén, M. 2007, MNRAS, 379, 260
- Mahdavi, A., Hoekstra, H., Babul, A., & Henry, J. P. 2008, MNRAS, 384, 1567
- Mahdavi, A., Hoekstra, H., Babul, A., et al. 2013, ApJ, 767, 116
- Mantz, A. B., Allen, S. W., Morris, R. G., et al. 2015, MNRAS, 449, 199
- McCarthy, I. G., Schaye, J., Bower, R. G., et al. 2011, MNRAS, 412, 1965
- Mohr, J. J., Fabricant, D. G., & Geller, M. J. 1993, ApJ, 413, 492
- Mohr, J. J., Mathiesen, B., & Evrard, A. E. 1999, ApJ, 517, 627
- Molnar, S. M., Hearn, N., Haiman, Z., et al. 2009, ApJ, 696, 1640
- Morandi, A., Sun, M., Forman, W., & Jones, C. 2015, MNRAS, 450, 2261
- Nagai, D., Kravtsov, A. V., & Vikhlinin, A. 2007, ApJ, 668, 1
- Nurgaliev, D., McDonald, M., Benson, B. A., et al. 2013, ApJ, 779, 112
- Oppenheimer, B. D., & Schaye, J. et al. 2013, MNRAS, 434, 1062
- Pfrommer, C., EnBlin, T. A., & Springel, V. 2008, MNRAS, 385, 1211
- Piffaretti, R., Arnaud, M., Pratt, G. W., Pointecouteau, E., & Melin, J.-B. 2011, A&A, 534, A109
- Poole, G. B., Fardal, M. A., Babul, A., et al. 2006, MNRAS, 373, 881
- Quilis, V., Planelles, S., & Ricciardelli, E. 2017, MNRAS, 469, 80
- Roediger, E., Kraft, R. P., Nulsen, P. E. J., et al. 2015, ApJ, 806, 103
- Roncarelli, M., Ettori, S., Dolag, K., et al. 2006, MNRAS, 373, 1339

- Rozo, E., Bartlett, J. G., Evrard, A. E., & Rykoff, E. S. 2014, *MNRAS*, 438, 78
- Rudnick, L., & Lemmerman, J. A. 2009, *ApJ*, 697, 1341
- Sanderson, A. J. R., Ponman, T. J., Finoguenov, A., Lloyd-Davies, E. J., & Markevitch, M. 2003, *MNRAS*, 340, 989
- Sanderson, A. J. R., Ponman, T. J., & O'Sullivan, E. 2006, *MNRAS*, 372, 1496
- Sanderson, A. J. R., Edge, A. C., & Smith, G. P. 2009, *MNRAS*, 398, 1698
- Santos, J. S., Rosati, P., Tozzi, P., et al. 2008, *A&A*, 483, 35
- Sarazin, C. L. 1988, *Cambridge Astrophysics Series*, Cambridge: Cambridge University Press, 1988,
- Schellenberger, G., Reiprich, T. H., Lovisari, L., Nevalainen, J., & David, L. 2015, *A&A*, 575, A30
- Snowden, S. L., Mushotzky, R. F., Kuntz, K. D., & Davis, D. S. 2008, *A&A*, 478, 615
- Strazzullo, V., Paolillo, M., Longo, G., et al. 2005, *MNRAS*, 359, 191
- Sun, M., Voit, G. M., Donahue, M., et al. 2009, *ApJ*, 693, 1142
- von der Linden, A., Allen, M. T., Applegate, D. E., et al. 2014, *MNRAS*, 439, 2
- Walker, S. A., Fabian, A. C., Sanders, J. S., Simionescu, A., & Tawara, Y. 2013, *MNRAS*, 432, 554
- Wang, Q. D., & Walker, S. 2014, *MNRAS*, 439, 1796
- Willingale, R., Starling, R. L. C., Beardmore, A. P., Tanvir, N. R., & O'Brien, P. T. 2013, *MNRAS*, 431, 394